Dynamics and reliability of bistable neurons driven with time-dependent stimuli

Soledad Gonzalo Cogno[1], Susanne Schreiber[2] and Inés Samengo[1]

1: Centro Atómico Bariloche and Instituto Balseiro, San Carlos de Bariloche, Argentina. 2: Institute for Theoretical Biology, Humboldt Universität zu Berlin and Bernstein Center for Computational Neuroscience, Berlin, Germany

Abstract:

The reliability of a spiking neuron depends on the frequency content of the driving input signal. Previous studies have shown that well above threshold, regularly firing neurons generate reliable responses when the input signal resonates with the firing frequency of the cell. Instead, well below threshold, reliable responses are obtained when the input frequency resonates with the subthreshold oscillations of the neuron. Previous theories, however, provide no clear prediction for the input frequency giving rise to maximally reliable spiking at threshold, which is probably the most relevant firing regime in mammalian cortex under physiological conditions. In particular, when the firing onset is governed by a subcritical Hopf bifurcation, the frequency of subthreshold oscillations often differs from the firing rate at threshold. The predictions of previous studies, hence, cannot be smoothly merged at threshold. Here we explore the behavior of reliability in bistable neurons near threshold using three types of driving stimuli: constant, periodic and stochastic. We find that the two natural frequencies of the system, associated to the two coexisting attractors, provide a rich variety of possible locking modes with the external signal. Reliability is determined by the sensitivity to noise of each locking mode, and also by the transition probabilities between modes. Noise increases the amount of spike-time jitter, and minimal jitter is obtained for input frequencies coinciding with the suprathreshold firing rate of the cell. In addition, noise may either enhance or inhibit transitions between the two attractors, depending on the input frequency. The dual role played by noise in bistable systems implies that reliability is determined by a delicate balance between spike-time jitter and the rate of transitions between attractors.

1 Introduction

In many brain regions, single neurons convey large amounts of information in the precise timing of individual spikes (Mainen and Sejnowsky, 1995). Spike timing is determined by two factors: the intrinsic properties of the spiking neuron and the temporal characteristics of the input currents. In cortical cells, the total input is a combination of localized synaptic inputs and large-scale fluctuating fields. The latter determine the local field potentials surrounding the cell, and their spectral characteristics strongly depend on the behavioral state of the subject (Buszáki, 2006). Since the frequency content of the driving signal has a profound impact on the reliability of neural activity (Tiesinga et al, 2008), it is important to understand which input frequency bands produce most reliable responses. This, of course, means to understand the interplay of intrinsic neuronal oscillatory properties and the extrinsic driving signal.

Previous studies have identified the input frequencies that induce reliable spiking in neurons driven by suprathreshold (Hunter et al., 1998; Schreiber et al., 2004) and subthreshold stimuli (Fellous et al., 2001; Schreiber et al., 2009). When the mean input current is above threshold, spiking is maximally reliable when the input frequency coincides with the firing rate frequency $f_{\rm fir}$. Below threshold, instead, the optimal input frequency is the subthreshold resonance $f_{\rm res}$, at least, for neurons whose resting state is governed by a spiral fixed point, characterized by a well-defined frequency (Izhikevich, 2007). When non-resonant neurons are driven with sinusoidal stimuli, the slower the stimulus, the more reliable the obtained response. These studies allow us to predict the reliability of neurons well above or well below threshold. From the physiological point of view, however, these extreme regimes are only marginally relevant. In realistic situations neurons are typically maintained close to threshold, in order to maximize their selectivity by firing intermittently. It is therefore important to extend previous studies in order to also encompass situations where cells fluctuate around threshold.

In non-resonant type 1 neurons the firing onset is governed by a saddle-node bifurcation on the invariant circle, and the optimal subthreshold frequency $f_{\rm res} = 0$ merges continuously with the optimal suprathreshold firing frequency $f_{\rm fir}$, since the latter vanishes at threshold. Neurons that pass to the firing state through a supercritical Hopf bifurcation also merge $f_{\rm res}$ into $f_{\rm fir}$ continuously, in both cases with frequencies larger than zero, and coinciding with the imaginary part of the eigenvalue losing stability. The situation is different, however, for models that undergo a subcritical Hopf bifurcation, since at threshold $f_{\rm res}$ is typically different from $f_{\rm fir}$, as exemplified in Fig. 1. Such models are often used to represent the firing threshold of several types of neurons, as stellate cells of entorhinal cortex, various interneurons (fast spiking,

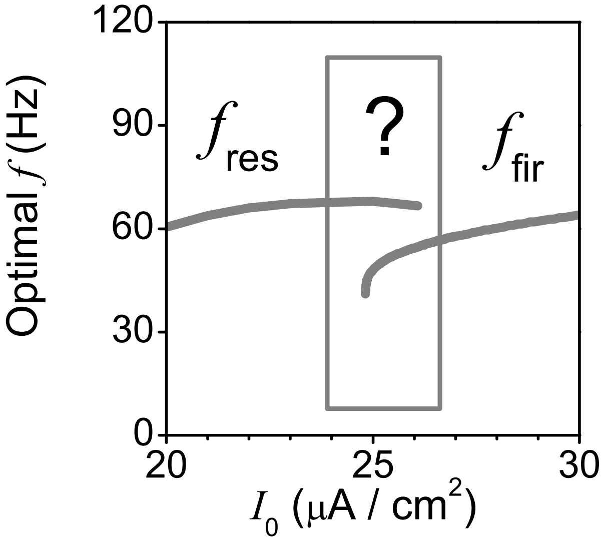

Figure 1: Optimal input frequency f predicted by previous theories, displayed as a function of the mean input current I_0, in a type II Morris Lecar model neuron. Firing onset is governed by a subcritical Hopf bifurcation. Well below threshold, the optimal f coincides with the subthreshold resonance of the cell f_{res}. Well above threshold, the optimal f coincides with the firing rate f_{fir}. The object of this paper is to reveal the optimal input frequency around the firing theshold.

late spiking and stuttering cells), reticular thalamic neurons and mesencephalic V neurons of brainstem (Izhikevich, 2007). Unfortunately, in these cases, previous theories do not give an unambiguous prediction of the value of the optimal input frequency.

Our goal is to analyze the frequency dependence of response reliability of neurons operating around their firing threshold. We work with a type II Morris Lecar neuron model containing a bistable zone at the firing onset. We observe that the degree of reliability depends in a complex way of the input frequency, the amplitude of the oscillatory component in the input signal, the amount of noise, the initial conditions, and the total recording time (Sect. 2). The complexity of the problem is explained through an analysis of the dynamical properties of the bistable system when driven with time-dependent stimuli, here developed in Sects. 3-6. These tools allow us to bridge the gap between the former supra- and subthreshold explorations, and extend them across the firing threshold.

2 Reliability in the bistable zone of Morris-Lecar neurons

For simplicity, we choose a 2-dimensional neuronal system. Similar results are obtained for higher-dimensional models with the same bifurcation structure at threshold (e.i., Hodgkin-

Huxley). The equations of the Morris-Lecar model are

$$
\begin{aligned}
C\frac{\mathrm{d}V}{\mathrm{d}t} &= -I_{\mathrm{ion}}(V,w) + I(t),\\
\frac{\mathrm{d}w}{\mathrm{d}t} &= -\frac{w - w_\infty(V)}{\tau_w(V)},
\end{aligned}
\tag{1}
$$

where $I_{\mathrm{ion}}(V,w) = g_{\mathrm{L}}(V - V_{\mathrm{L}}) + g_{\mathrm{Ca}}(V - V_{\mathrm{Ca}}) + g_{\mathrm{K}} w(V - V_{\mathrm{K}})$, and other parameters as in Schreiber et al. (2009). In order to study the frequency dependence of reliability, we model the input current $I(t)$ as

$$I(t) = I_0 + I_1\ \sin(2\pi f t) + I_{\mathrm{noise}}(t), \tag{2}$$

where I_{noise} is Gaussian white noise with

$$\langle I_{\mathrm{noise}}(t)\ I_{\mathrm{noise}}(t')\rangle = \sigma^2\ \delta(t - t'). \tag{3}$$

All simulations were performed with a stochastic second order Runge-Kutta integration routine (Honeycutt, 1992), and integration step $\mathrm{d}t = 0.1$ ms, which is approximately 20 times smaller than the passive characteristic time of the membrane C/g_{L}.

To measure the degree of reliability, we run the system of Eqs. 1 a large number of trials (500 or 1000) always with the same initial conditions and oscillatory input, but independent realizations of the noisy term I_{noise}. We evaluate reliability by estimating the degree of synchronization between trials (Golomb and Rinzel, 1993, 1994)

$$\chi^2 = \frac{\mathrm{Var[psth(t)]}}{\langle \mathrm{Var[r_i(t)]}\rangle_i}, \tag{4}$$

where $r_i(t)$ is a binary string representing trial i, containing a 1 in every time bin where a spike was generated, and a 0 otherwise. In this paper, we parse the spike train in time bins of duration 1 ms. In Eq. 4, Var represents the temporal variance, and $\mathrm{psth(t)} = \langle r_i(t)\rangle_i$ is the trial average of binary strings. The value of χ^2 is an estimate of the fraction of synchronized trials, and when it drops below the inverse of the total number of trials, spike generation is completely unreliable. The results presented here remain essentially unchanged when other reliability measures are employed (e.g., Schreiber et al., 2003).

When the value of I_0 is chosen so that the neuron is at threshold, and inside the bistable regime, reliability depends strongly on the input frequency f, the amplitude I_1 of the sinusoidal stimulus, the amount of noise σ, the initial conditions (suprathreshold or subthreshold) and the amount of stimulation time, as illustrated in Fig. 2. Several questions arise from this figure. What does the complex vertical structure represent? Why do some regions of the plane (f, I_1) become more reliable, and others less reliable, when the stimulation time is increased? When

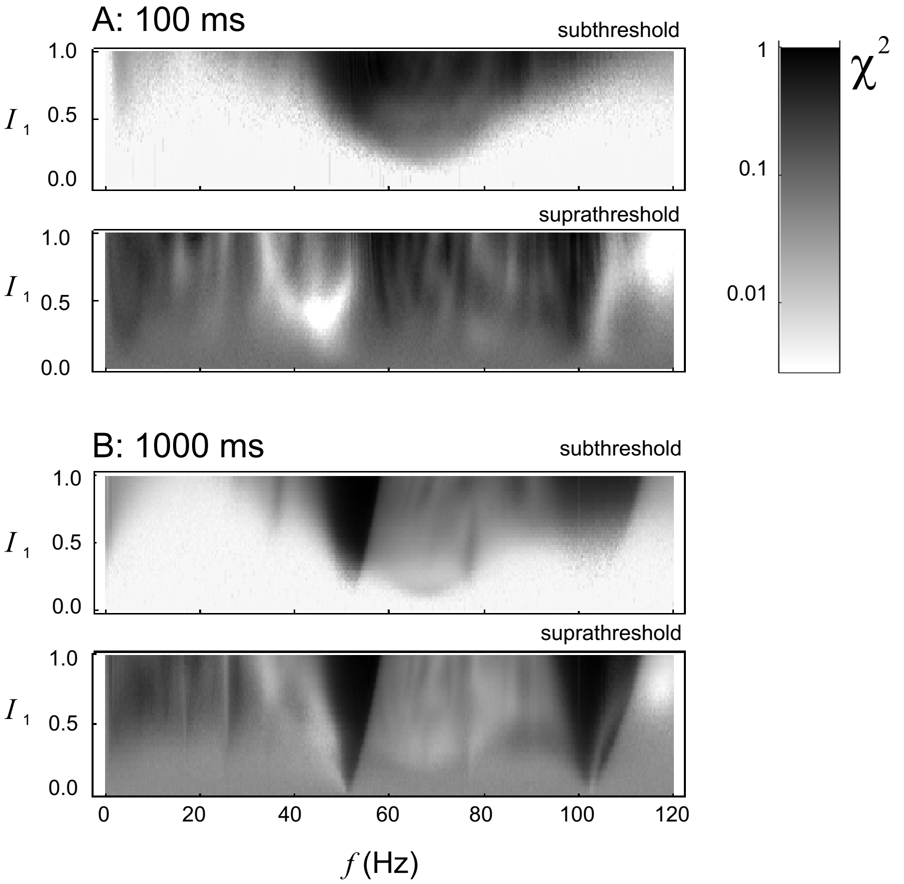

Figure 2: Reliability χ^2 in a Morris Lecar model neuron driven with sinusoidal input current (Eq. 2) of amplitude I_1 (in μA/cm^2) and frequency f. Mean stimulus $I_0 = 25.4\mu$A/cm^2 and amount of noise $\sigma = 0.3\mu$Ams$^{1/2}$/cm^2). Different gray levels indicate different reliability values, from perfectly reliable (black) to completely unreliable (white). The areas where no spikes are generated appear in white. *A*: Total stimulation time: 100 ms. *Top panel*: subthreshold initial conditions: $V(t = 0) = -21.35$ mV, $w(t = 0) = 0.2$. *Bottom panel*: suprathreshold initial conditions: $V(t = 0) = 4.65$ mV, $w(t = 0) = 0.43$.*B*: Total stimulation time: 1000 ms. Initial conditions: same as in A. Right: greyscale of χ^2.

and why do initial conditions matter? In the bottom panel of Fig. 2A, why do we see confined regions where reliability goes to zero? In order to answer these questions, we explore the dynamical properties of the Morris Lecar neuron in simpler contexts. In Sect. 3 we describe the autonomous case ($I_1 = 0$ and $\sigma = 0$). In Sect. 4, we incorporate a noisy term to the input current ($I_1 = 0$, $\sigma > 0$); in Sect. 5 we return to the noiseless situation, but we add an oscillatory component to the input ($I_1 > 0$, $\sigma = 0$); and finally, in Sect. 6 we consider the fully complex case of Fig. 2 ($I_1 > 0$, $\sigma > 0$).

3 Bistability in the autonomous type II Morris-Lecar neuron model

In this section, the external input current $I(t)$ is taken to be constant, and equal to I_0. In Fig. 3A - 3C, the noiseless system is described. In Fig. 3A, the maximal and minimal voltage amplitudes of the invariant trajectories are displayed as a function of I_0. The frequency of oscillation along these trajectories is shown in Fig. 3B. The number of invariant trajectories and their stability

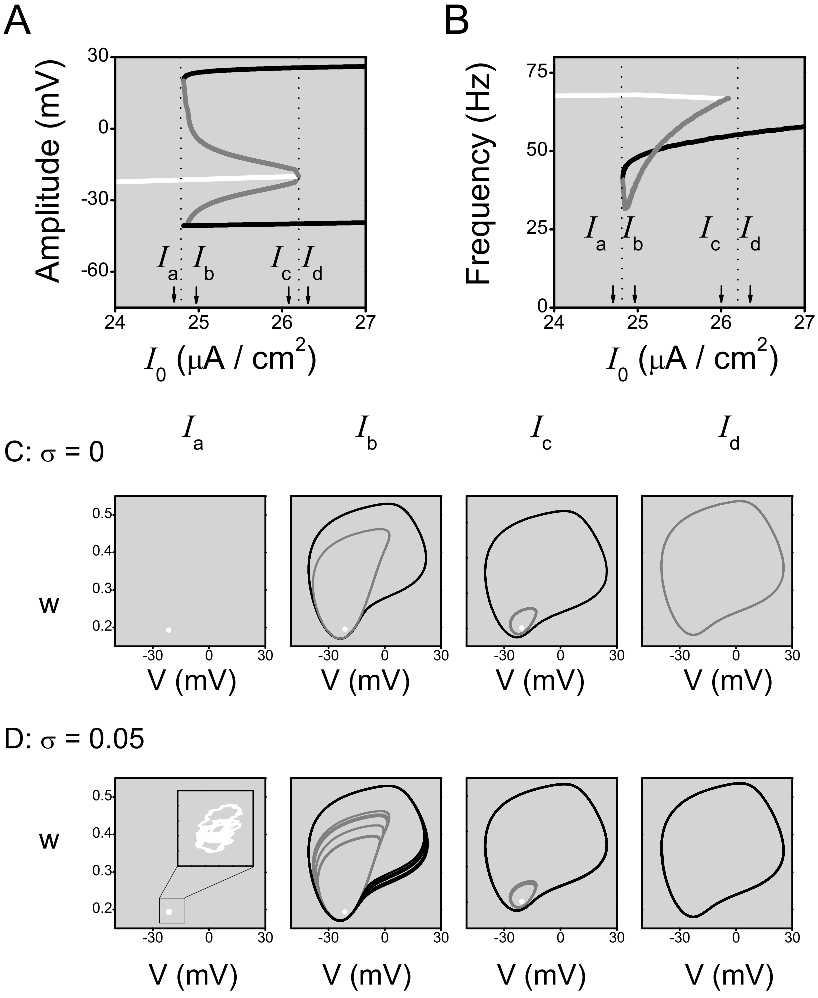

Figure 3: Invariant trajectories of the autonomous Morris-Lecar neuron model ($\sigma = 0$, panels A - C), and their noisy version (panel D, with $\sigma > 0$). *A*: Maximal and minimal voltage amplitudes of invariant trajectories, as a function of I_0. White: resting subthreshold fixed point. Grey: unstable limit cycle. Black: stable firing limit cycle. *B*: Frequency of the invariant trajectories, as a function of I_0. Line conventions: same as in A. *C*: Phase-space invariant trajectories for $\sigma = 0$ in the three different firing regimes: subthreshold ($I_0 = I_a = 24.8\mu$A/cm^2), bistable ($I_0 = I_b = 24.87\mu$A/cm^2 and $I_0 = I_c = 25.6\mu$A/cm^2), and suprathreshold ($I_0 = I_d = 26.3\mu$A/cm^2). *D*: Same as C, but with $\sigma = 0.05\mu\text{A ms}^{1/2}/\text{cm}^2$.

depends on the value of I_0. Trajectories in phase space are shown in Fig. 3C.

For $I_0 < 24.82 \mu\mathrm{A/cm}^2$ (case I_a), only a single invariant trajectory exists: a spiral fixed point, corresponding to the resting subthreshold state. The voltage component of this point is given by the white line in Fig. 3A. For all initial conditions, the system circles counter-clockwise down to the fixed point, giving rise to damped voltage oscillations. Asymptotically, the voltage fluctuations have zero amplitude, so the maximal and minimal amplitudes shown in white in Fig. 3A coincide. The frequency associated to the angular movement around the fixed point is around 68 Hz, and depends only mildly on I_0 (Fig. 3B). This frequency defines the subthreshold resonance f_{res} of the cell. It can be obtained analytically by linearizing the system of Eqs. (1) around the fixed point, and taking the imaginary part of the associated eigenvalue.

When I_0 is increased beyond $24.82 \mu\mathrm{A/cm}^2$ (case I_b), two limit cycles (in Fig. 3C, the stable one displayed in black, and the unstable one, in gray) appear in a distant region of phase space. The stable cycle constitutes the firing attractor, and the frequency of oscillation around this cycle is the firing rate f_{fir}. Since the unstable limit cycle is virtually never observed (trajectories depart away from it), we constructed the unstable trajectories of Fig. 3C by running the system backward in time. As I_0 is increased further (case I_c), the unstable limit cycle shrinks down towards the stable fixed point, colliding with it at $I_0 \approx 26.23 \mu\mathrm{A/cm}^2$, and inverting the stability of the remaining fixed point. Hence, within the range $I_0 \in [24.82, 26.23] \mu\mathrm{A/cm}^2$, the system has three invariant trajectories: the stable fixed point (white), the unstable limit cycle (grey), and the firing limit cycle (black). The amplitude of the unstable limit cycle diminishes continuously (Fig. 3A) connecting the two stable attractors, and so does the frequency (Fig. 3B).

The unstable invariant trajectory constitutes a boundary (also called *separatrix*) between the basins of attraction of the resting state and the firing cycle: All initial conditions that lie inside the separatrix evolve towards the resting state, whereas those that start outside approach the firing limit cycle. Later on, when when we add a noisy term I_{noise} to the input signal, transitions between the two attractors will become possible. The only portion of the limit cycle that comes close to the fixed point is at the bottom of the orbit, when w reaches its minimum value. Transitions will typically take place in this particular region of phase space (Rowat and Greenwood, 2011).

For $I_0 > 26.23 \mu\mathrm{A/cm}^2$ (case I_{d}), the resting state is no longer stable, and the only attractor of the system is the firing limit cycle. In this case, all initial conditions tend rapidly towards the black trajectory.

4 Dynamics of the noise-driven system

In Fig. 3D, the input current contains a noisy component ($\sigma > 0$). For the small value of σ depicted here, trajectories in phase-space retain many of the properties discussed for the autonomous case. Still, the time-dependent system described by Eqs. (1) is no longer autonomous, so now trajectories often intersect each other. In the purely subthreshold regime, the resting state is no longer a fixed point (see the enlarged inset for I_a), although trajectories still tend to remain confined to a small region whose diameter is proportional to the amount of noise σ. Around the fixed point, noisy trajectories have a roughly elliptic shape, and the power spectrum of $V(t)$ has a sharp peak at frequency f_{res}. Therefore, when small amounts of noise are injected into the system, the fixed point of the autonomous case is transformed into a stochastic subthreshold trajectory with main revolution frequency f_{res}.

When $\sigma > 0$, the critical values of I_0 defining the borders of the bistable region may differ from the ones of the unperturbed case. Still, for small σ, for some I_0 in the neighborhood of $24.82\mu\mathrm{A}/\mathrm{cm}^2$, the transition to bistability takes place. Due to the non-stationarity of Eqs. (1), now both the firing limit cycle and the unstable cycle occupy broad regions of phase space, crossing their own paths, as well as other trajectories. In any case, as long as σ remains small, the main features of the autonomous system remain: The unstable limit cycle shrinks down towards the subthreshold trajectory, and eventually, after the collision of the two, the only stable attractor of the system is the firing limit cycle.

4.1 Transient and stationary firing rate

The coexistence of two stable attractors in the noiseless case has important consequences for the behavior of the noisy system. In the absence of noise, both the fixed point and the stable limit cycle have basins of attraction. If the system is initially in one of the basins, it inevitably evolves towards the corresponding attractor. Strictly speaking, the concept of basins of attraction no longer holds when noise is incorporated. Although the system may initially be in the basin of one of the attractors (for example, the fixed point), noise may induce transitions to the other basin (the limit cycle). The probability of transitions depends on the amount of noise σ, the geometry and location of the attractors (determined by I_0), and on the direction of the jump (from suprathreshold to subthreshold, or vice versa).

Example raster plots are displayed in Fig. 4A, for suprathreshold (top) and subthreshold

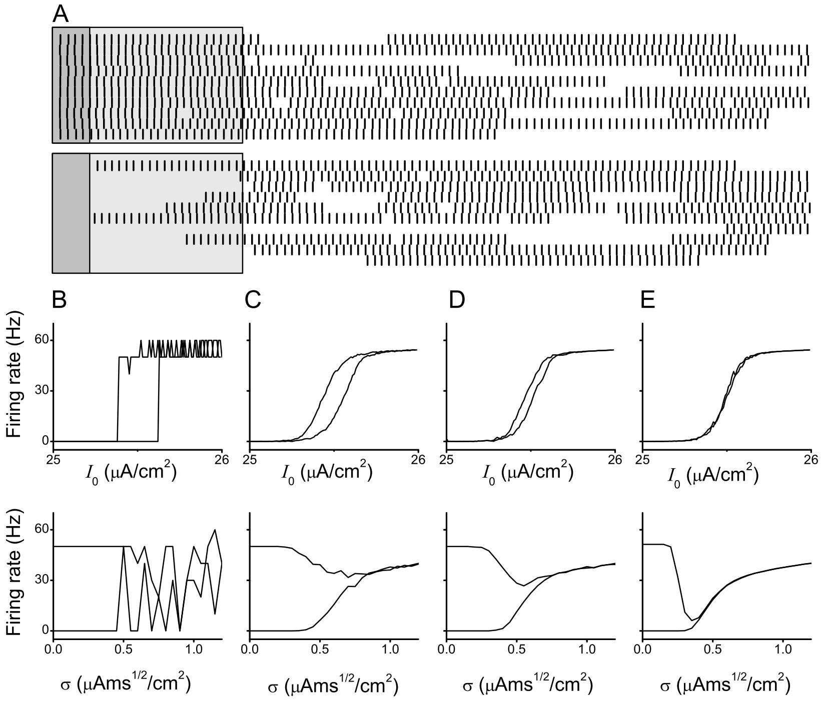

Figure 4: Variation of mean firing rates with initial conditions and total recording time. *A*: Raster plot for different noise samples, for 10 supra-threshold initial conditions (top) and 10 sub-threshold initial conditions (bottom). $I_0 = 25.5\mu$A/cm^2, $\sigma = 0.4\mu$Ams$^{1/2}$/cm^2. Total time: 2000 ms. The rectangles indicate the time windows used to measure firing rates in panels *B* and *C* (100 ms) and *D* (500 ms). *B*: Single-trial firing rates measured in a 100 ms time window, as a function of I_0 for $\sigma = 0.4\mu$ A ms$^{1/2}$ / cm^2 (top), and as a function of σ for $I_0 = 25.4\mu$A/cm^2 (bottom). The two curves in each panel correspond to sub- and suprathreshold initial conditions. *C*: Same as *B*, but each point is obtained by averaging 200 cells with independent noise samples. *D*: Same as *C*, but now using a 500 ms time window to compute the rates. *E*: Same as *B*-*D*, but now using a 25,000 ms time window.

(bottom) initial conditions. When the system is in the basin of attraction of the limit cycle, spiking takes place at a fairly regular rate. Transitions to the basin of the fixed point appear as blank periods in raster plots. No intermediate rates are observed. When suprathreshold initial conditions are used, the trial starts in the firing state, whereas subthreshold conditions begin in the quiescent state.

In Fig. 4B we see the firing rate obtained for a single trial in a 100 ms time window. The top panel is constructed by slowly increasing I_0, and recording the number of produced spikes, and then slowly decreasing I_0 to the starting value. The two obtained curves form a hysteresis cycle describing the behavior obtained for subthreshold and suprathreshold conditions. In the particular run of Fig. 4B, subthreshold initial conditions produce quiescent behavior, and suprathreshold conditions produce regular firing. The firing state may contain either 5 or 6 spikes in the 100 ms recording window, depending on the noise sample. Hence, in the upper panel of Fig. 4B, the firing state contains fluctuations between 50 and 60 Hz. In the lower panel, the firing rate is depicted as a function of σ, for sub and suprathreshold initial conditions. As σ grows, transitions between the (former) fixed point and the limit cycle become increasingly frequent, and the system immediately loses memory of its initial state. Hence, for $\sigma > 0.5\mu$Ams$^{1/2}$/cm^2, the two curves coalesce.

However, a single run does not suffice to characterize the properties of the system, because the critical values of I_0 and σ where transitions take place depend on the particular noise sample at hand. Other noise samples may shift these values. Therefore, in Fig. 4C we show the same curves as in Fig. 4B, but averaged among 500 noisy cells. The population average eliminates the jagged behavior, giving rise to continuous curves. One should remember, however, that no intermediate firing rates are observed in single cells. In Fig. 4D, the analysis is repeated, but now rates are computed in a time window that is 5 times as long (500 ms). In the lower panel of Fig. 4C and, more notably, Fig. 4D, the suprathreshold curve exhibits an inverse stochastic resonance a function of σ (Tuckwell and Jost, 2010; Tuckwell et al, 2009). Several parameters determine the shape of these curves, as the size of the (transient) bistable zone (upper panel), and the depth of the minimum defining the inverse resonance (lower panel). These parameters, however, vary with the length of the recording window. For a long time window, we obtain the results in Fig. 4E. In this example, in the upper panel (measured with $\sigma = 0.4\mu$Ams$^{1/2}$/cm^2), the curves corresponding to sub- and suprathreshold initial conditions coalesce, so the window can be considered long enough to estimate stationary firing rates. However, for smaller σ values, even the 25-second window employed here is not enough to reach stationarity, as can be seen in the lower panel. For all $\sigma > 0$, one can find a recording window that is sufficiently long such that there be no difference between the curves obtained with supra or subthreshold initial conditions, and hysteresis be lost. After the first transition between attractors, the system can no longer remember its initial state. If the system has time to switch between attractors a large number of times, the average fraction of time spent in each basin is independent of initial conditions. One would therefore expect that in the limit of infinite time, the suprathreshold curve in the lower panel of Fig. 4E would coincide with the subthreshold curve, except for a discontinuity at $\sigma = 0$, where the firing rate of the suprathreshold system should always be equal to frequency of the noiseless limit cycle. Hence, in the limit, both bistability and inverse stochastic resonance disappear. For low noise, however, the stationary situation is only reached after unrealistically long waiting times. We must therefore characterize not only the stationary situation, but also the transient ones.

4.2 Transition rates between attractors

In the previous section, we saw that mean firing rates strongly depend on the duration of the recording window. In order to obtain a stationary value, the window has to be long compared to the rate of transitions between the two coexisting attractors. In this section, we study such transition rates, showing that sometimes they oscillate periodically in time. We also analyze their dependence on the amount of noise σ.

In Fig. 5A we show the inter-spike interval (ISI) distribution $P(\tau)$ estimated from the histogram obtained in a 50000-spike run. We see a sharp peak at the origin, and a long, exponential tail (Rowat and Greenwood, 2011), indicating that some silences can last for even more than 6 seconds - an extremely long period in the subthreshold state. The inset displays the details of the distribution near the origin. Several peaks can be seen. The first and most prominent one is located at $\tau = 19.5$ ms, coinciding with the inverse of the frequency of the firing limit cycle at the selected I_0. Subsequent peaks are separated by 16 ms, only slightly longer than the inverse of the frequency of the subthreshold oscillation frequency. The regular sequence of peaks implies that firing either occurs after a single turn around the firing limit cycle (first peak), or after one turn around the firing limit cycle that before completion is interrupted by a transition to the subthreshold state, where an arbitrary number of turns around the subthreshold fixed point follow. Eventually, another transition to the suprathreshold state takes place, the interrupted turn is completed, and a spike is generated. The regular sequence of peaks in the inset of Fig. 5A implies that transitions only occur at integer multiples of the period of the subthreshold state $f_{\rm res}^{-1}$, at least, during the first few turns, when the influence of noise is still not enough to corrupt the coherence of the quasi-periodic motion around the limit cycle. These observations are in agreement with previous analyses of trajectories in phase space (Rowat and Greenwood, 2011), demonstrating that transitions occur at a precise location in phase space, where the periodic orbit approaches the fixed point.

The distinction between firing and silent periods implies that neurons generate bursts of spikes. In the absence of noise, Morris Lecar neurons do not burst. Therefore, the bursting observed here is due to the transitions between attractors induced by noise. The minimum separating the first two peaks of the ISI distribution defines a limiting ISI $\tau_{\rm lim}$, which can be used to determine whether a given ISI of duration τ was generated in the subthreshold regime (if $\tau > \tau_{\rm lim}$), or in the suprathreshold regime (if $\tau < \tau_{\rm lim}$). The average sub- and suprathreshold ISIs are depicted in Fig. 5B. We see that suprathreshold ISIs remain markedly invariant throughout a wide range of σ values. Instead, subthreshold ISIs vary by several orders of magnitude. Each

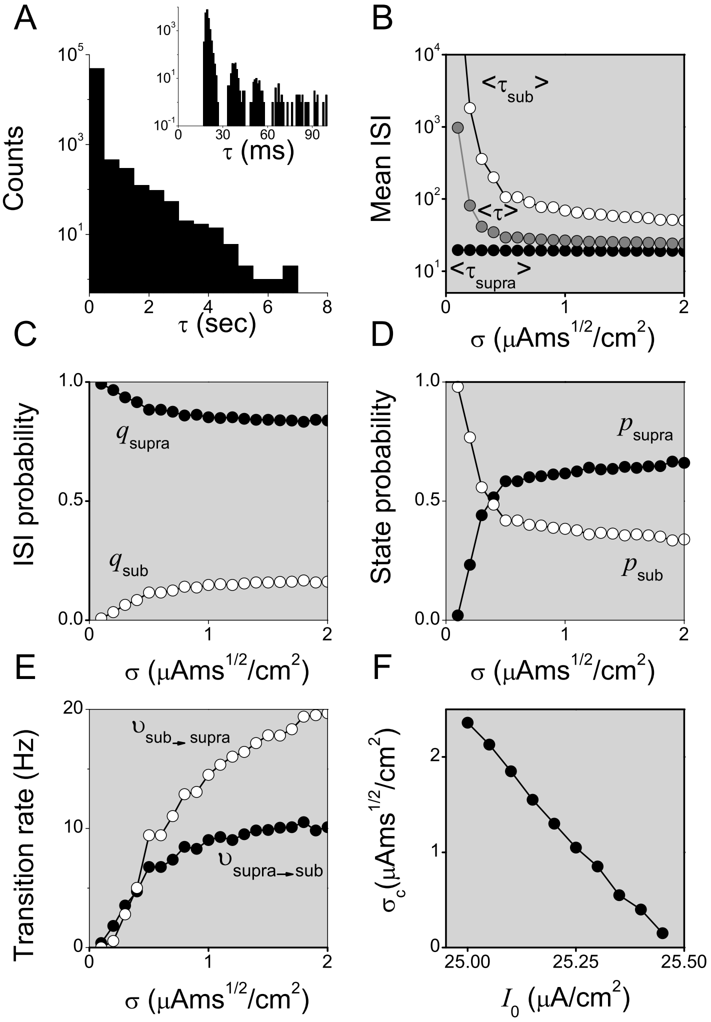

Figure 5: Statistics of the transitions between the two stable attractors. *A*: ISI histogram obtained in a run of 50000 spikes, $I_0 = 25.4\mu$A/cm^2, $\sigma = 0.5\mu$A ms$^{1/2}$/cm^2. Other panels: simulations with 5000 spikes. *B*: Mean ISI in ms; supra-threshold ($\langle\tau_{\rm supra}\rangle$), sub-threshold ($\langle\tau_{\rm sub}\rangle$), and total $\langle\tau\rangle$.*C*: Ratios $q_{\rm supra}$ and $q_{\rm sub}$ of the number of supra or subthreshold ISIs and the total number of ISIs. *D*: Probabilities $p_{\rm supra}$ and $p_{\rm sub}$ of finding the system in a supra or subthreshold state, at any given time (Eq. 5). *E*: Transitions probabilities per unit time $\nu_{\rm supra\to sub}$ and $\nu_{\rm sub\to supra}$ (Eqs. 6 and 7). *F*: Dependence of $\sigma_{\rm c}$, defined as the noise level at which the two transition rates are equal, with the mean current I_0. Black symbols: suprathreshold state, or transitions from the supra to the subthreshold state. White symbols: subthreshold state, or transitions from the sub to the suprathreshold state. The discrepancy between the results obtained with different initial conditions was smaller than the size of the symbols.

subthreshold ISI contains a variable number of turns around the fixed point. The average number of turns decreases as σ increases, because noise favors transitions, and thereby, forestalls long silent intervals.

We now define the quantities that allow us to measure transition rates between attractors. If

$\langle\tau\rangle$ is the average ISI, and p_{supra} and p_{sub} are the probabilities that at any given time the system be found in the supra or subthreshold regimes, then

$$\begin{aligned} p_{\mathrm{supra}} &= \frac{1}{\langle\tau\rangle}\int_0^{\tau_{\mathrm{lim}}} P(\tau)\,\tau\,\mathrm{d}\tau, \\ p_{\mathrm{sub}} &= \frac{1}{\langle\tau\rangle}\int_{\tau_{\mathrm{lim}}}^{+\infty} P(\tau)\,\tau\,\mathrm{d}\tau. \end{aligned} \tag{5}$$

We call q_{supra} and q_{sub} the ratio between the number of supra- and subthreshold ISIs relative to the total number of ISIs, respectively. In order to derive the transition rates $\nu_{\mathrm{supra}\to\mathrm{sub}}$ and $\nu_{\mathrm{sub}\to\mathrm{supra}}$, we discretize time in small intervals of duration δt. We define the rate $\nu_{\mathrm{supra}\to\mathrm{sub}}$ as the ratio between the number of bins immediately preceding a transition to the subthreshold state and the total number of bins in the suprathreshold state. The total number of bins in the suprathreshold state is equal to the total amount of time spent in the suprathreshold state divided by the bin size, that is, $p_{\mathrm{supra}} N\langle\tau\rangle/\delta t$, where N is the total number of ISIs. Out of this number, Nq_{sub} bins terminate the suprathreshold state, inducing a transition to the subthreshold state. Therefore,

$$\nu_{\mathrm{supra}\to\mathrm{sub}} = \frac{q_{\mathrm{sub}}}{p_{\mathrm{supra}}}\,\frac{1}{\langle\tau\rangle}. \tag{6}$$

In order to derive the rate of transitions from the subthreshold state to the suprathreshold state, we follow an analogous argument, replacing p_{supra} by p_{sub}. Note that q_{sub} should not be replaced by q_{supra}, because the total number of transitions is always $q_{\mathrm{sub}}N$, irrespective of the direction of the transition. Hence,

$$\nu_{\mathrm{sub}\to\mathrm{supra}} = \frac{q_{\mathrm{sub}}}{p_{\mathrm{sub}}}\,\frac{1}{\langle\tau\rangle}. \tag{7}$$

Combining Eqs. 6 and 7, we arrive at the balanced state relation

$$p_{\mathrm{supra}}\,\nu_{\mathrm{supra}\to\mathrm{sub}} = p_{\mathrm{sub}}\,\nu_{\mathrm{sub}\to\mathrm{supra}}, \tag{8}$$

implying that if transitions in one direction occur at a higher rate than in the opposite direction, then the system must spend proportionally longer periods of time in the favored state.

Subthreshold ISIs last for a long time, but are few in number. This is shown in Fig. 5C, where the probabilities q_{supra} and q_{sub} are displayed. If one chooses an ISI at random, the probability of selecting a suprathreshold ISI are substantially larger than that of a subthreshold one - more so, if σ is small. This does not imply, however, that the system spends more time in the suprathreshold state, since subthreshold ISIs can be very long. The probabilities p_{supra} and p_{sub} that at any given time the system be found in the supra or subthreshold states are displayed in Fig. 5D. For small σ, most of the time is spent in the subthreshold state. At about $\sigma = 0.4\mu$Ams$^{1/2}$/cm^2 the two transition rates become equal, so for even larger noise levels, the suprathreshold state dominates.

When the system is in a suprathreshold state, the probability per unit time to switch to the subthreshold state is $\nu_{\text{supra}\to\text{sub}}$. This transition rate, together with the complementary $\nu_{\text{sub}\to\text{supra}}$, is displayed in Fig. 5E. Both rates increase substantially as σ grows. Initially, the transition rate from supra to sub is larger, and at approximately $\sigma = 0.4\mu$Ams$^{1/2}$/cm^2, the situation reverses.

As mentioned earlier, an inspection of trajectories in phase space reveals that transitions typically occur near the point where the limit cycle approaches the fixed point. That is, at two specific phases along the suprathreshold and subthreshold trajectories. The fact that the rate $\nu_{\text{sub}\to\text{supra}}$ be larger than $\nu_{\text{supra}\to\text{sub}}$ does not necessarily mean that, at the specific point in phase space where transitions take place, noise is more effective in inducing the upward transition than the downward one. There is another factor at play, namely, that oscillations around the fixed point are faster than those around the limit cycle, and therefore, there are more occasions per unit time to go from subthreshold to suprathreshold than the other way round. To address this point, in addition to the transition probabilities *per unit time*, we can calculate the transition probabilities *per unit switching occasion* $\mu_{\text{supra}\to\text{sub}}$ and $\mu_{\text{sub}\to\text{supra}}$. These probabilities represent the likelihood to make a transition each time the system passes through those phases where switches are possible. They are related to the transition rates by

$$\begin{aligned} \mu_{\text{supra}\to\text{sub}} &= \nu_{\text{supra}\to\text{sub}} \times t_{\text{supra}} \\ \mu_{\text{sub}\to\text{supra}} &= \nu_{\text{sub}\to\text{supra}} \times t_{\text{sub}}, \end{aligned} \tag{9}$$

where t_{supra} and t_{sub} are the inverse of the natural frequencies of the firing limit cycle and the spiral fixed point, respectively, for the chosen I_0 (14.8 ms and 19.4 ms in the case of Fig. 5). These probabilities bear the same dependence with the amount of noise σ as the transitions rates ν, although they are always scaled between 0 and 1.

The value $\sigma_{\text{c}} = 0.4\mu$ A ms$^{1/2}$/cm^2 constitutes a border in the scale of noise levels. Below the border, the subthreshold state dominates, and above, the suprathreshold one. The critical noise level σ_{c} required to equate the transition rates depends on the continuous stimulus component I_0, which was fixed to 25.4 μA/cm^2 in Fig. 5A-E. In Fig. 5F we show that σ_{c} is approximately linear with I_0 with a slope of $\approx$ -5 ms$^{1/2}$. As I_0 varies inside the bistable region, the critical amount of noise required to equate the amount of time spent in the sub and suprathreshold states diminishes.

The aim of this section was to develop a criterion to determine whether a given recording window was short or long. When the window is shorter than the inverse of the transition rate $\nu_{\text{supra}\to\text{sub}}$, all evolutions initiated in the suprathreshold state are likely to remain suprathreshold during the entire trial. The same conclusion holds for the subthreshold case. Initial conditions, hence, are expected to become irrelevant only when the duration of the recording window is substantially longer than both transition rates, so that a good sampling of transitions in both directions are guaranteed to be included. If the recording time is shorter, then different scenarios are possible. For example, if the recording time is larger than $\nu^{-1}_{\text{supra}\to\text{sub}}$ but shorter than $\nu^{-1}_{\text{sub}\to\text{supra}}$, the system is effectively in the subthreshold regime, because it has time to switch to the subthreshold state, but not enough to return to the suprathreshold one. In these conditions, the curve of firing frequency as a function of I_0 (as in Fig. 4) appears shifted to the right, such that the region where the two attractors coexist appears for larger I_0 values.

5 Dynamics of the noiseless, sinusoidally-driven system

In order to assess the frequency dependence of reliability, we need to drive the system with time-dependent stimuli. Hence, we now stimulate the Morris-Lecar neuron with a deterministic, time-dependent current of well-defined frequency f, momentarily eliminating the noisy term I_{noise}. The non-stationary nature of $I(t)$ again allows for crossing trajectories in phase space, as seen in Fig. 6A. In the subthreshold regime, the resting state is no longer a fixed point, it is now a small elliptic trajectory traversed at the frequency of the external signal f. The size of the ellipse depends on f. In the neighborhood of the (former) fixed point, the system of Eqs. 1 can be linearized and solved completely for an oscillatory input current as in Eq. 2. The size and shape of the stationary elliptic trajectory (reached after a brief transient evolution) can be obtained analytically. In Fig. 6B we display the length of the major and minor axes as a function of the input frequency. Maximal amplitude is obtained for $f \approx 68$ Hz, that is, when the external frequency coincides with the resonance frequency, the latter defined as the imaginary part of the eigenvalue of the fixed point of the autonomous system (see Fig. 3B). The ellipse in the inset of the lower and leftmost panel of Fig. 6A is therefore larger than the ellipse obtained with any other frequency.

When I_0 crosses the critical current of the global bifurcation, a stable limit cycle appears (black curve in Fig. 6A). For small I_1, the firing limit cycle is traversed at approximately 50 Hz. If $f \approx 50$ Hz, the limit cycle is even more stable and has larger attracting capacity than in the autonomous case. As f departs from 50 Hz (and its harmonics), the disruptive effect of the external signal grows. In the trajectories of Fig. 6A, the disruptive effect is evidenced in a certain instability in the location of the lower right part of the limit cycle, when $I_0 = I_b$. There, the trajectory wobbles, due to the impossibility to lock the external signal at 68 Hz with the

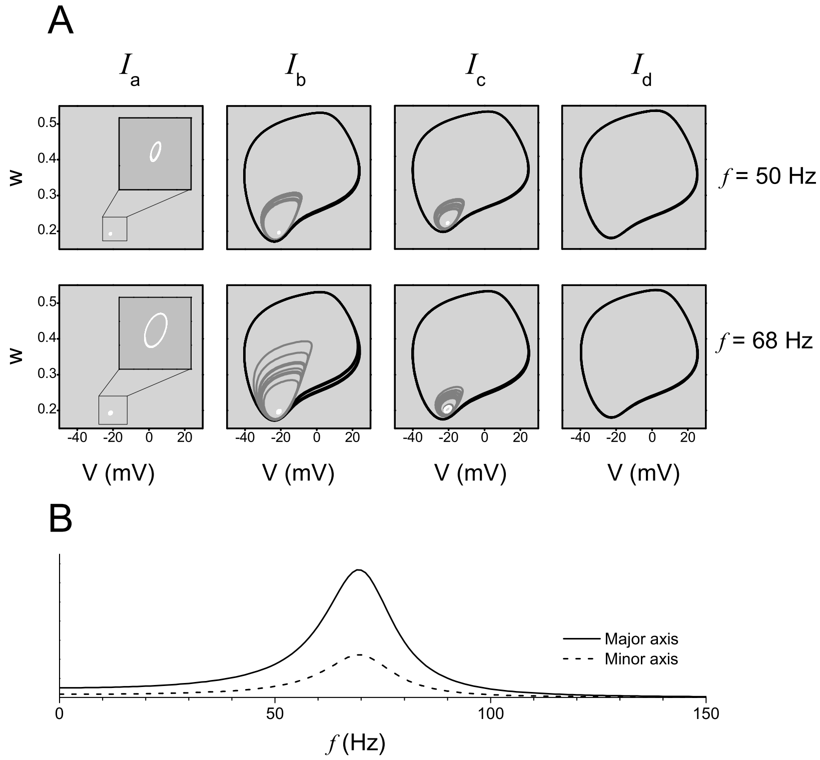

Figure 6: Properties of selected trajectories in the Morris-Lecar neuron model driven with sinusoidal input (Eq. 2), with $I_1 = 0.1\mu$ A/cm^2. *A*: Phase-space invariant trajectories in the three different firing regimes: subthreshold ($I_0 = I_a = 24.8\mu$A/cm^2), bistable ($I_0 = I_b = 25.1\mu$A/cm^2 and $I_0 = I_c = 25.6\mu$A/cm^2), and suprathreshold ($I_0 = I_d = 26.3\mu$A/cm^2). Line conventions: same as in Fig. 3. *First row*: $f = 50$ Hz. *Second row*: $f = 68$ Hz. *B*: Analytical calculation of the frequency dependence of the size of the major and minor axes of the subthreshold ellipse.

circulation frequency at 50 Hz. The same happens with the unstable trajectory (gray). Finally, when I_0 is larger than the critical current for the bifurcation of the fixed point, the resting cycle is no longer attractive, and all trajectories approach the firing limit cycle.

The notion of purely subthreshold or suprathreshold trajectories only holds for input stimuli where the oscillating component is small, as illustrated in Fig. 7. In the left column (Fig. 7A), we see that as I_1 increases (i.e., as we move down in the graph), the width of the bistable zone shrinks, and for $I_1 \geq 0.4\mu$ A/cm^2, it disappears completely. The voltage traces are shown in Fig. 7B, as a function of time. As I_1 grows, the amplitude of the trajectory corresponding to subthreshold initial conditions (white) increases. In these trajectories, the voltage oscillates with the frequency of the external input (43.5 Hz), which in this example is slower than the spiking frequency (50 Hz) of the trajectory with suprathreshold initial conditions (black). For $I_1 \geq 0.4\mu$ A/cm^2 the distinction between subthreshold or suprathreshold trajectories is lost, since both initial conditions give rise to trajectories that switch back and forth between a 43.5 Hz, small-

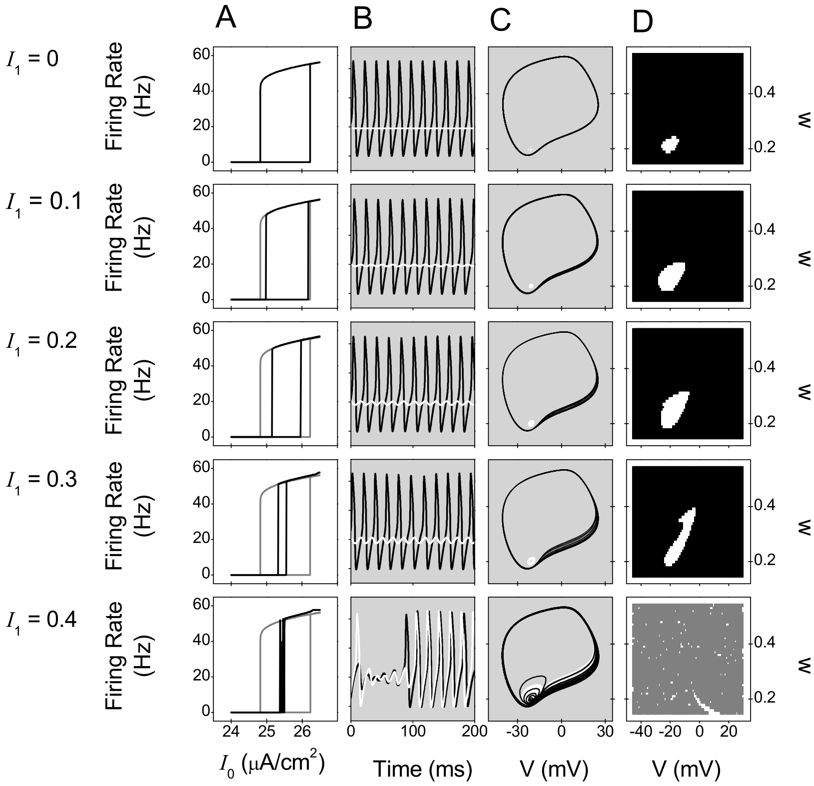

Figure 7: Effect of the amplitude I_1 of the sinusoidal stimulus component. Input frequency: $f = 43.5$ Hz. I_1 values indicated in μ A / cm^2. *A*: Firing rate as a function of the continuous stimulus component I_0. The firing rate corresponding to the autonomous case $I_1 = 0$ is shown in gray also in the lower panels. *B*: Voltage traces as a function of time, with suprathreshold (black) and subthreshold (white) initial conditions. Scale of ticks in the vertical axes: 20 mV. *C*: Phase-space trajectories obtained with suprathreshold (black) and subthreshold (white) initial conditions. *D*: Basins of attraction of the subthreshold state (white) and suprathreshold firing cycle (black). In the last panel, the initial conditions corresponding to trajectories that switch back and forth between the two attractors are displayed in gray.

amplitude oscillation around the (former) fixed point, and a 50 Hz, large-amplitude oscillation around the firing trajectory. The same effect is evident in the phase-space trajectories of Fig. 7C. In D, we show the basins of attraction of the subthreshold state (white) and suprathreshold firing cycle (black). As I_1 grows, the basin of attraction of the subthreshold state becomes increasingly enlarged and distorted, approaching the limit cycle. At a certain I_1, the two basins coalesce, so trajectories that have started in the subthreshold area are able to reach the limit cycle, and vice versa. Depending on the input frequency, trajectories may either become purely suprathreshold, or switch back and forth between the two attractors, as in the last row of Fig. 7D. The few isolated initial conditions that remain subthreshold, do so only for a specific choice of the initial phase of the oscillating component of the sinusoidal stimulus. Therefore, for large I_1, almost no trajectories can be classified into purely subthreshold or suprathreshold.

The effects displayed in Fig. 7 remain qualitatively unchanged when we vary the input frequency f. There are, however, quantitative differences. When the input frequency is near $f_{\rm res} \approx 68$ Hz, the size of the subthreshold basin of attraction is particularly large. Therefore, even a relatively small sinusoidal amplitude I_1 suffices to enlarge the subthreshold basin so that it coalesces with the suprathreshold basin, allowing trajectories to reach the limit cycle. Instead, when the input frequency is near to $f_{\rm fir} \approx 50$ Hz, the firing cycle is particularly robust, and the basin of the subthreshold state is comparatively small. Hence, a large I_1 is required for the latter to be able to touch the former. These effects are systematically explored in Fig. 8. In panel A, we see that when $f = f_{\rm fir}$, the bistable region has a square shape, implying that the firing frequency is fixed at 50 Hz, roughly independently of I_0. The width of the bistable zone, moreover, increases with the amplitude I_1, so that when I_1 grows, the global bifurcation generating the stable and unstable limit cycles appears for smaller I_0 values. The oscillatory component, hence, does not challenge the stability of the limit cycle. On the contrary, it enhances it. The subcritical Hopf bifurcation that annihilates the fixed point, instead, is relatively unsensitive to I_1.

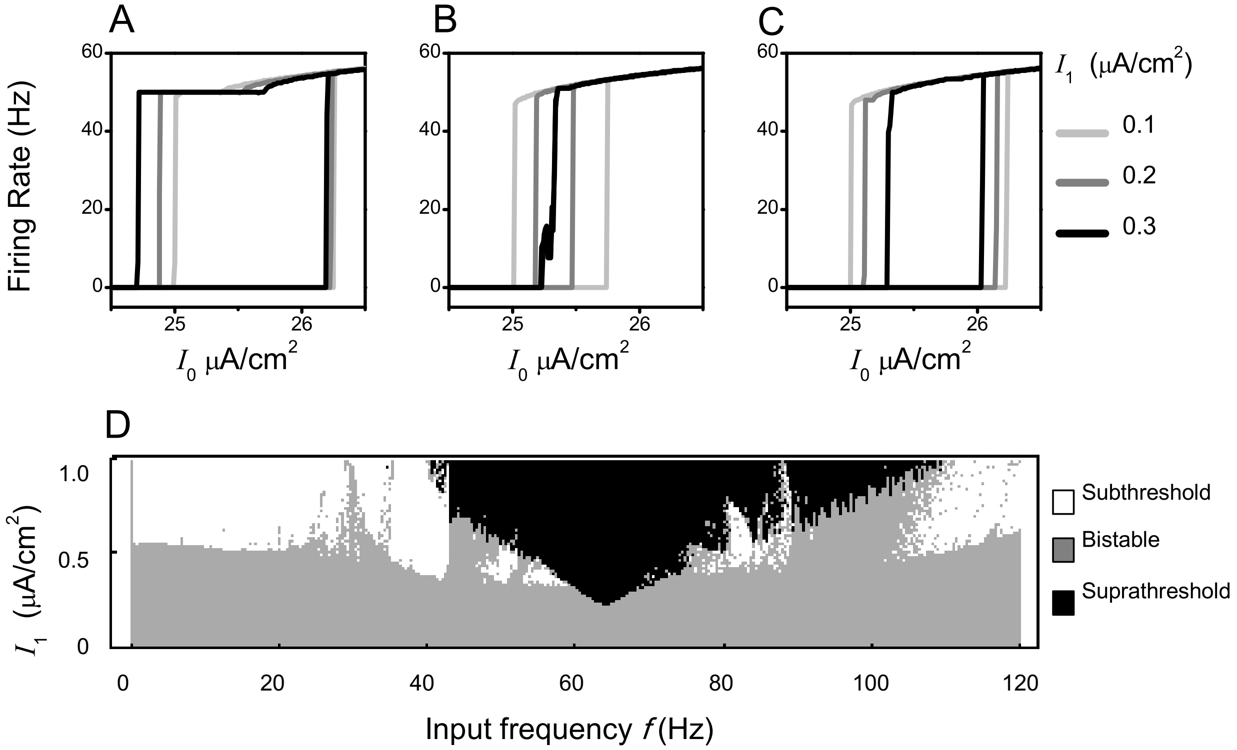

Figure 8: Size and location of regions of bistability depend on stimulus frequency and amplitude. *A*-*C*: Firing rate as a function of the continuous component of the input I_0, for several stimulation frequencies and sinusoidal amplitudes. *A*: $f = 50$ Hz. *B*: $f = 68$ Hz. *C*: $f = 80$ Hz. *D*: Classification of trajectories into three categories: purely suprathreshold (black, all initial conditions give rise to spiking), purely subthreshold (white, all intitial conditions give rise to quiescent behavior), and bistable (gray, some initial conditions result in spiking, and others in quiescent behavior). I_0 = 25.6 μA/cm^2.

For other input frequencies, the width of the bistable zone always decreases with I_1. When $f = f_{\mathrm{res}}$ (Fig. 8B), the bistable zone shrinks particularly rapidly. A smaller effect is observed when f is far away from f_{fir} and f_{res} (Fig. 8C). Hence, bistability is particularly robust when the input frequency coincides with the firing rate frequency (Fig. 8A), and particularly fragile when it coincides with the resonance frequency of the subthreshold state (Fig. 8B), other cases showing an intermediate behavior.

In Fig. 8D we explore the types of trajectories that can be encountered with different combination of input frequency f and sinusoidal amplitude I_1. When all initial conditions give rise to quiescent behavior, the corresponding (f, I_1) point is displayed in white. When all initial conditions give rise to spiking (that may be either regular or irregular, depending on whether occasional tours around the fixed point are interleaved), the point is shown in black. When suprathreshold initial conditions give rise to firing and subthreshold ones produce quiescent behavior, the point is in gray. To construct the figure, for each pair (f, I_1), we adiabatically increased I_0 from a clearly subthreshold value (22 μA/cm^2) up to the target value (25.4 μA/cm^2). The adiabatic increase ensured that, if the fixed point was stable at the target I_0, we would always remain near the fixed point, and therefore, we would be able to start the simulation with subthreshold initial conditions. At the target I_0, we evaluated whether the system spiked or remain quiescent, and thereby, determined whether the fixed point still existed. Next, we adiabatially decreased I_0 from a clearly suprathreshold value (28 μA/cm^2) up to the target value (25.4 μA/cm^2), and evaluated whether spikes were generated or not. We thereby determined whether the stable limit cycle still existed.

A prominent black tongue is seen at around 65 Hz, that is, near the frequency of the subthreshold resonance. Therefore, at these frequencies, comparatively small sinusoidal amplitudes I_1 suffice to push the (large) subthreshold trajectory into the region occupied by the firing limit cycle, giving rise to spiking even for subthreshold initial conditions.

Black areas in Fig. 8D represent cases where all initial conditions give rise to firing, but provides no information about the firing rate. Whenever the system switches back and forth between the two attractors, the average firing rate falls below 50 Hz. In order to identify the switching cases, in Fig. 9A and B we display the mean firing rate of the cell in each point of the (f, I_1) plane, for sub and suprathreshold initial conditions. Initial conditions were searched with the same adiabatic procedure of Fig. 8D.

The central black tongue of Fig. 8D at 65 Hz appears as the region where spikes are generated with subthreshold initial conditions in Fig. 9A. Within the tongue, however, a large variety

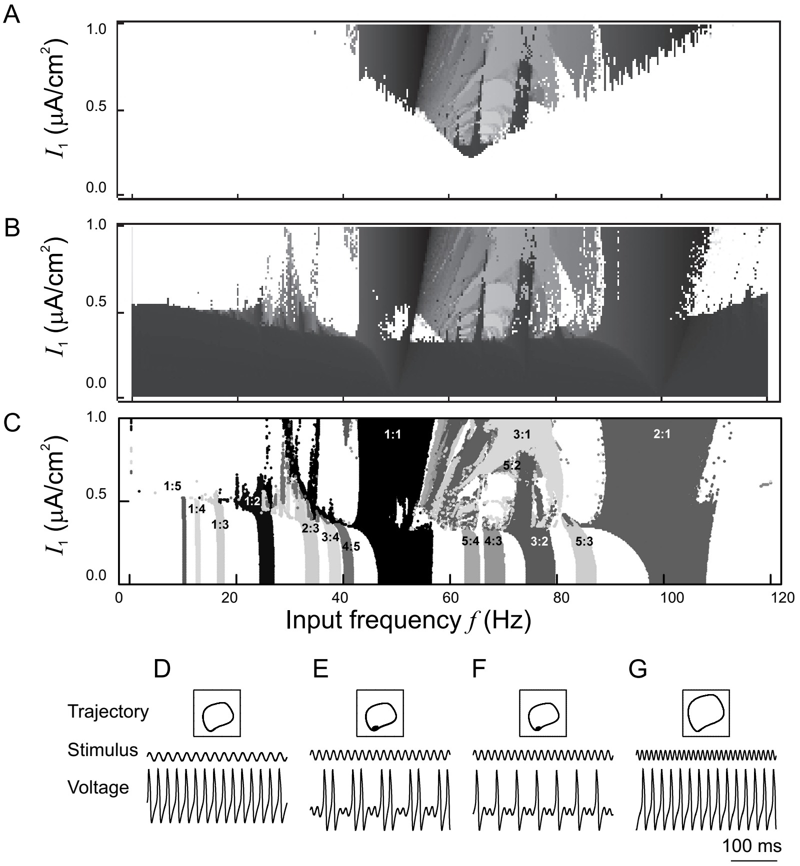

Figure 9: Structure and complexity of the firing states of the sinusoidally driven, noiseless system. $I_0 = 25.4\mu$A/cm^2 (bistable regime, in the autonomous system). *A*: Mean firing frequency for subthreshold initial conditions. *B*: Mean firing frequency for suprathreshold initial conditions. Dark areas correspond to 50 Hz firing. Lighter areas alternate circulation around the limit cycle and the subthreshold attractor. White regions contain no spikes. *C*: Locking modes $n : m$, where n stimulus cycles occur in the same interval as m spikes. Each area represents the region in the (f, I_1) space where the firing rate differs from nf/m in less than 10% of the amount that would be required to be confounded with neighboring modes $n \pm 1 : m$ or $n : m \pm 1$. *D-G*: Example trajectories and applied stimulus displayed as a function of time. In all cases, $I_1 = 0.8\mu$A/cm^2. *D*: $f = 50$ Hz, locking (1:1). *E*: $f = 65$ Hz, locking (4:2), *F*: $f = 70$ Hz, locking (3:1), *G*: $f = 100$ Hz, locking (2:1). Insets: Trajectories in phase space. X axis: V. Y axis: w.

of firing rates appear in stripes, building a complex structure in the (f, I_1) plane. Dark areas represent regular 50 Hz firing, as exemplified in Fig. 9D. Lighter regions represent alternating trajectories, where the system skips periodically or aperiodically between the two attractors (see examples in panels E-F). The firing rate of trajectories starting with suprathreshold conditions (Fig 9B) coincides with the one obtained with subthreshold conditions inside the central tongue (Fig. 9A). The complexity of these maps embodies all the mode-locking states that the system can have, as found also in previous studies (Coombes and Bressloff 1999; Coombes and Owen 2001; Laing and Longtin 2003; Tiesinga 2002; Borkowski 2010, 2011). In Fig. 9C, we see the regions where the firing frequency is maintained at a fixed proportion (indicated by the numbers) of the input frequency. Notice that one same proportion may correspond to more than a single locking pattern. For example, at $I_1 = 0.8\mu$A/cm^2 two different locking modes (shown in red) are obtained for $f = 65$ Hz and $f = 100$ Hz (see panels E and F), and in both cases, the stimulus frequency is twice the firing rate. Many of the striped structures in the locking map coincide with the structures in the firing rate maps. Hence, complex locking patterns induce complex firing-rate patterns.

When the external frequency is similar to f_{fir}, the circulation speed around the limit cycle is adapted so that the firing rate is locked to the external frequency. Circulation along the lowest portion of the cycle (when w reaches its minimum value) occurs when the stimulus reaches its maximum value. Hence, the region where transitions occur is traversed with maximal speed. This effect will become important later on, when we add noise to the system. A similar situation is found when f is an integer multiple of f_{fir}.

As f departs from f_{fir}, locking can no longer take place by adapting the circulation speed inside the cycle. If $f \approx f_{\text{res}}$, transitions between attractors become likely, so many locking modes based on periodically switching trajectories are possible. These interlacing locking modes give rise to the complicated structures in the central frequency band of Fig. 9A-C.

At low amplitudes ($I_1 < 0.2\mu$A/cm^2), the system is essentially bistable, and the presence of the sinusoidal component has little impact in the firing rate. Above this amplitude, if f is far away from both f_{fir} and f_{res}, locking becomes difficult. For large I_1, when $f < f_{\text{fir}}$, the input signal oscillates slower than the firing rate. Therefore, circulation around the limit cycle is unstable, since the whole cycle wobbles back and forth in phase space along the horizontal direction, with frequency f. If the amplitude of the wobbling movement is sufficiently large, the firing trajectories cross the subthreshold basin, and the system cannot escape from the quiescent state. At this point, the system becomes entirely subthreshold (see white areas in Figs. 9A and B). Only with higher I_0 values can firing be recovered.

6 Bistability in the presence of both noise and sinusoidal input

In Fig. 10 we display the spike trains obtained when the input current contains both the oscillatory and the noisy components ($I_1 > 0$ and $\sigma > 0$ in Eq. 2). Two very different behaviors can

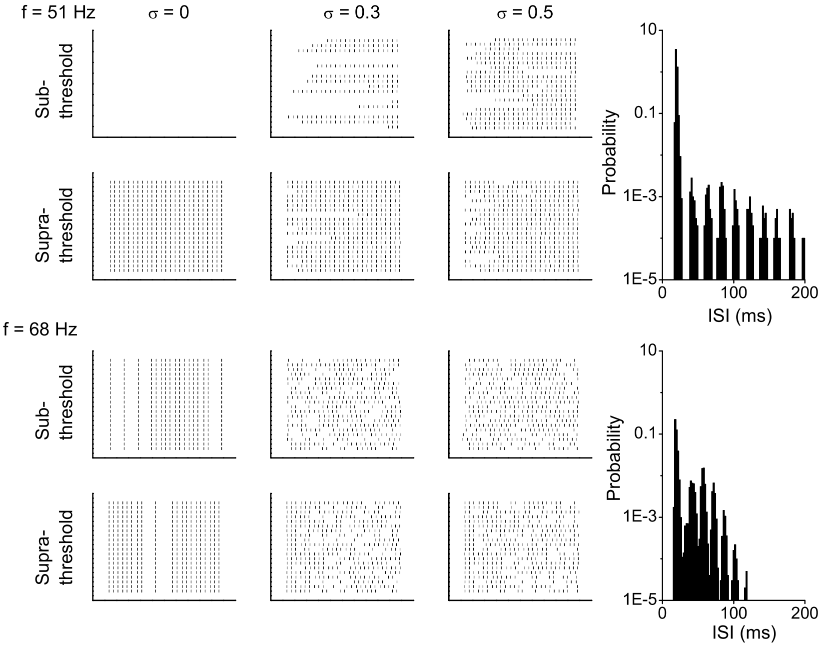

Figure 10: Spike trains obtained when both an oscillating and a noisy term are included in the input current. Simulation time: 500 ms. Top: $f = 51$ Hz. Bottom: $f = 68$ Hz. Different columns correspond to different σ values expressed in μAms$^{1/2}$/cm^2. Right: ISI distributions for $\sigma = 0.5$ μAms$^{1/2}$/cm^2. In all panels, I_0 = 25.5 μ A / cm^2, and $I_1 = 0.5 \mu$ A / cm^2.

be seen, depending on whether f is near to $f_{\rm res}$ or to $f_{\rm fir}$. If $f \approx 50$ Hz, markedly different spike trains are obtained when we start with sub or with suprathreshold initial conditions. A comparatively large amount of noise is needed to induce transitions between the two attractors, and silent periods tend to be long, as evidenced by the long tail in the ISI distribution. Noticeably, during the firing periods, spike trains are remarkably regular even when noise is comparatively large, with almost no visible evidence of spike-time jitter. Noise, hence, seems to be necessary to induce transitions, but has almost no effect in shifting individual spikes.

Contrasting with the case of $I_1 = 0$ (see Fig. 5A), now the multiple peaks in the ISI distribution are all separated by ≈ 20 ms, with no distinction between the first peak and the subsequent ones. When $f = 50$ Hz, both the subthreshold elliptic trajectory and the firing limit cycle are circulated at 50 Hz. Hence, if each ISI represents one full turn around the limit cycle and an arbitrary number of turns around the fixed point, ISIs are necessarily integer multiples of 20 ms.

When $f \approx 68$ Hz, instead, even the noiseless system ($\sigma = 0$) fluctuates between the two attractors (Fig. 9C), giving rise to both spikes and silent periods. Comparatively small amounts of noise introduce numerous stochastic transitions between the two attractors and also give rise to spike-time jitter. The ISI distribution contains a first peak at 19 ms, approximately corresponding to the 50 Hz firing observed in the stretches when the system generates several spikes in the suprathreshold state. Subsequent peaks, however, are separated by 15 ms, corresponding to an oscillation of approximately 68 Hz. When $f = 68$ Hz, the subthreshold ellipse is traversed at 68 Hz. However, the limit cycle is still traversed at 50 Hz. Hence, if each ISI represents one full turn around the limit cycle and an arbitrary number of turns around the fixed point, peaks are necessarily separated by 15 ms intervals.

The resting state is more susceptible to the external frequency than the firing state: The subthreshold ellipse is circulated at the frequency of the external current, whereas the limit cycle remains at $f_{\rm fir}$, unless the oscillatory amplitude I_1 is increased substantially. Therefore, for any input current different from $f_{\rm fir}$, the separatrix divides phase space into two regions of conflicting frequencies. The conflict is particularly noticeable if $f = f_{\rm res}$, since for this frequency, the ellipse is large. The subthreshold trajectory is hence pushed very near of the limit cycle, and small amounts of noise suffice to induce transitions.

The high transition rates obtained with $f \approx f_{\rm res}$ and the low ones for $f \approx f_{\rm fir}$ are also evident in the slope of the the exponential envelope of the tail of the ISI distribution. The flat tail observed for $f = 50$ Hz, and the steep one for $f \approx f_{\rm res}$, imply that the transition rate $\nu_{\rm sub \to supra}$ is larger (Rowat and Greenwood, 2011).

In Fig. 11, we show the dependence of the transition rates on the amount of noise σ and the input frequency f. In the first row of A we see that when the oscillatory component is small ($I_1 = 0.3\mu$A/cm^2) two general observations can be made: (a) For large amounts of noise $\nu_{\rm sub \to supra}$ is always larger than $\nu_{\rm supra \to sub}$, and (b), the two transition rates increase monotonically with the amount of noise. From these two points we may conclude that noise tends to increase transitions in both directions and for all frequencies, but the transition $\rm sub \to supra$ is more enhanced than $\rm supra \to sub$. In essence, noise favors the suprathreshold state. In addition, for small amounts of noise, $\nu_{\rm sub \to supra}$ tends to zero, and does so more rapidly than $\nu_{\rm supra \to sub}$. This implies that the system spends most of the time in the subthreshold state. The exception is given by an input frequency $f \approx f_{\rm res}$, for which even in the noiseless case both transition rates are different from zero. This is because with this frequency, the system switches between attractors even in the absence of noise.

It is easy to build an intuitive picture where noise favors transitions. Less intuitive, however, is the behavior obtained when the oscillatory component is larger ($I_1 = 0.7\mu$A/cm^2). In the second row of panels of Fig. 11A, we see that noise may either increase, decrease, or leave the transition rates unaffected, depending on the input frequency. To understand this behavior, we

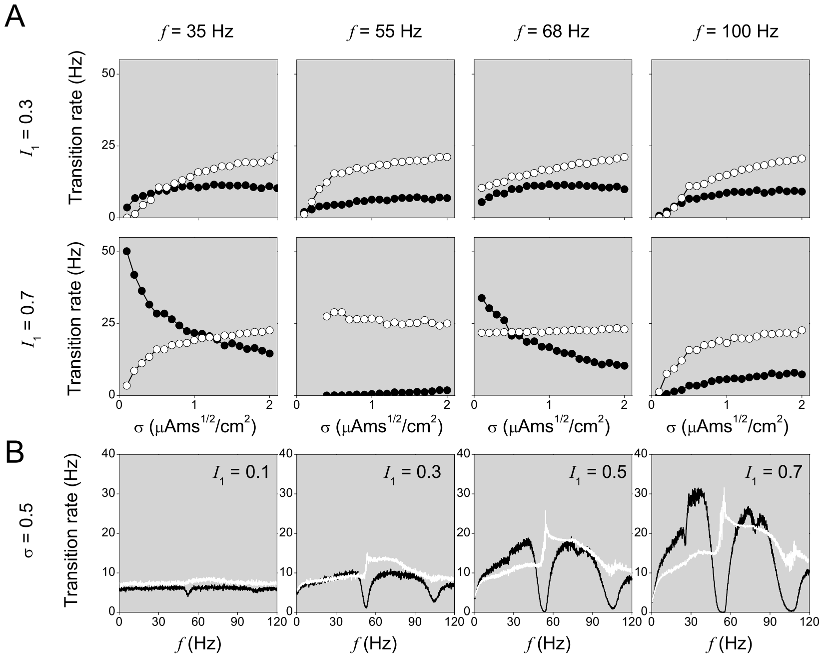

Figure 11: Dependence of the transition rates $\nu_{\mathrm{supra}\to\mathrm{sub}}$ (black) and $\nu_{\mathrm{sub}\to\mathrm{supra}}$ (white) on stimulus parameters. For all data points, $I_0 = 25.4\mu$ A / cm^2, and the stimulus was applied until 5000 spikes were obtained. *A*: Transition rates as a function of input noise, for four different input frequencies. Top: $I_1 = 0.3\mu$A/cm^2. Bottom: $I_1 = 0.7\mu$A/cm^2. *B*: Transition rates as a function of input frequency, for four different amplitudes I_1. The amount of noise σ is fixed at 0.5μA ms$^{1/2}$/cm^2.

recall the results of Fig. 9. For those frequencies where the system already switched between attractors even for $\sigma = 0$, transitions may actually be suppressed by noise. Such is the case for $f = 68$ Hz, in the third panel of the second row of Fig. 11A. Transitions $\mathrm{supra} \to \mathrm{sub}$ become less likely when noise increases, and the inverse transitions remain essentially unaffected. The asymmetry between the two directions is due to the fact that noise has a larger impact in perturbing trajectories along the limit cycle, that are already somewhat unstable, than around the fixed point, that is stabilized by the resonating input signal.

The transition rates $\nu_{\mathrm{supra}\to\mathrm{sub}}$ also decrease with σ when $f = 35$ Hz. In this case, the noiseless system is entirely in the subthreshold state, due to the large-amplitude, horizontal wobbling movement of the limit cycle. In the noiseless system, downward transitions occur almost immediately, whereas upward transitions never occur. Increasing the amount of noise, hence, can only suppress transitions $\mathrm{supra} \to \mathrm{sub}$, and enhance those $\mathrm{sub} \to \mathrm{supra}$.

If $f \approx f_{\mathrm{fir}}$ the suprathreshold state dominates at all noise levels. Transitions to the firing state are frequent, whereas transitions to the subthreshold state are rare. The difference between the transition rates in both direction is due to the fact that when $f \approx f_{\mathrm{fir}}$, circulation around the limit cycle is synchronized to the external signal. Hence, every time the system passes through the transition phase (below the fixed point), the external signal is positive and has maximum strength, pulling the trajectory maximally to the right. This force, supplied at this particular phase, is optimal to jump from the fixed point to the limit cycle, but not the other way round. This argument only holds for $f \approx f_{\rm fir}$ (or its harmonics). Any other input frequency is not synchronized with the circulation around the limit cycle, so the external force may be either positive or negative as the system passes through the transition phase. Consequently, the rectification effect is lost.

For $f = 100$ Hz, the noiseless system is bistable. Hence, the addition of noise produces qualitatively the same effect observed with smaller amplitude.

Figure 11B displays the dependence of the transition rates with the input frequency, when the amount of noise is fixed. We see that for small amplitudes, transition rates are roughly independent of f, with only a mild suppression of the transition $\rm supra \to sub$ for $f \approx f_{\rm fir}$. As I_1 grows, however, the dependence on the input frequency increases. For large amplitudes, the dynamics at $f = f_{\rm fir}$ (and its harmonics) is entirely suprathreshold (the black curve goes to zero). For $f \approx f_{\rm res}$ the two transition rates remain approximately equal, due to the switching trajectories. For slow input frequencies (frequencies for which the system becomes purely subthreshold in the noiseless case), noise allows occasional transitions to the suprathreshold state, though such events become less and less likely as I_1 grows.

7 Frequency-dependence of reliability in bistable neurons

The dynamical tools explored in the previous sections can now be used to understand the question posed in Fig. 1, and the unresolved issues raised in Fig. 2. According to previous studies (Hunter et al., 1998; Fellous et al., 2001; Schreiber et al., 2004; Schreiber et al., 2009), in the purely subthreshold regime (small I_0) maximal reliability is obtained when the input frequency coincides with $f_{\rm res}$. In the purely suprathreshold case (large I_0), instead, the optimal frequency is $f_{\rm fir}$. The object of the present study is to explore the reliability of neural responses when I_0 is in the bistable regime. The result of such explorations is summarized in Fig. 12.

Reliability in the bistable zone is not a straightforward interpolation between the sub- and supratheshold results. In Fig. 12 we see that reliable zones (displayed in dark) mainly appear at $f_{\rm fir}$ and its first harmonic. However, a complex structure of stripes is also visible, most

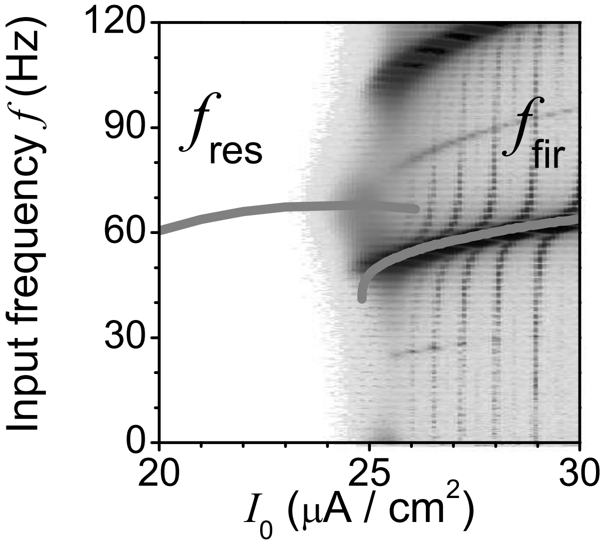

Figure 12: Reliability χ^2 as a function of the input frequency f and the mean stimulus I_0, for the same neuron as in Fig. 1. When I_0 is near the subthreshold range ($\approx 23\mu$A/cm^2), the cell only fires when $f \approx 68$ Hz. In the bistable range, a complicated structure of blotches appears. Well above threshold, firing is maximally reliable at $f = f_{\rm fir}$. Number of trials: 500; I_1 = 0.5 μA/cm^2; σ = 0.5 μA/cm^2 ms$^{1/2}$; recording time: 500 ms. Suprathreshold initial conditions, obtained by adiabatially approaching the measured I_0 from above.

notoriously, two intermediate frequencies (horizontal lines), and a number of preferred I_0 values (vertical lines). In these zones, the system has a strong locking mode, stabilized by the input signal. Unreliable zones (lighter areas) appear through two different mechanisms. First, noise can introduce temporal jitter, anticipating or delaying the timing of a given spike. Second, noise can induce transitions between attractors, introducing prolonged silences. The relevance of each of these factors depends on the stimulus frequency.

Reliability when $f \approx f_{\rm fir}$

When $f \approx f_{\rm fir}$, input noise has little effect in introducing spike-time jitter, for the same reasons that previous studies identified in the fully suprathreshold regime. The locking between the circulation around the limit cycle and the sinusoidal input component makes firing particularly robust. Previous studies have shown that when the firing threshold is traversed with a steeper voltage slope, spike-time jitter diminishes (Bryant and Segundo, 1976; Cecchi et al., 2000). Hence, reliability is high because for $f \approx f_{\rm fir}$, jitter is minimal.

In addition, for moderate or strong amplitudes I_1, transitions $\rm sub \rightarrow supra$ occur at a high rate, whereas the inverse transitions $\mathrm{supra} \to \mathrm{sub}$ virtually never occur. The point in phase space where transitions are likely to occur is locked to maximal sinusoidal stimulation. Therefore, the time interval where noise is capable of inducing transitions is reduced, and the system remains almost always in the suprathreshold state. Hence, for $f \approx f_{\mathrm{fir}}$ reliability is high also due to the fact that there are almost no missing spikes, and increasing noise levels have only a marginal effect.

Reliability when $f \approx f_{\mathrm{res}}$

There are situations, however, where $f \approx f_{\mathrm{fir}}$ may not be the optimal input frequency, since the system may not be able to reach the limit cycle. If the amplitude I_1 is small, the amount of noise σ is small, and the system is initially in the subthreshold state, reaching the limit cycle involves a transition $\mathrm{sub} \to \mathrm{supra}$. This transition is much more likely when $f \approx f_{\mathrm{res}}$ than with $f \approx f_{\mathrm{fir}}$. Recall from Fig. 11 that when $\sigma \to 0$, the transition rate $\nu_{\mathrm{sub}\to\mathrm{supra}} \to 0$ for $f \approx f_{\mathrm{fir}}$, implying that infinite long times are required to jump to the limit cycle. This transition rate, however, remains approximately at 10 Hz for $f \approx f_{\mathrm{res}}$, so 100 ms should suffice. As a consequence, in Fig. 2, for subthreshold initial conditions an $I_1 < 0.2\mu$A/cm^2, reliability vanishes for all input frequencies except $f \approx f_{\mathrm{res}}$, where χ^2 remains at a small, nonzero value. In this regime, firing is structured as an alternation of circulations around the limit cycle at frequency f_{fir}, and around the fixed point at frequency f_{res}. The alternation between attractors introduces a rich variety of locking modes, that allow the system to accommodate the trajectory to the external frequency. This situation allows noise to be highly effective in introducing spike-time jitter and transitions to the subthreshold state, since minor perturbations often suffice to shift the phase of these complex trajectories. As unreliable as these responses may be, they are still more reliable than no spiking at all, or than spiking every several seconds.

Dependence of reliability on the initial state, and on the length of the recording window

Even when starting with suprathreshold initial conditions, reaching a locked state typically takes several turns around the limit cycle. For short recording windows, in many trials the system may not have enough time to accommodate its circulation phase to reach entrainment with the external signal. During the initial transient cycles the system may or may not be highly sensitive to noise, depending on the relative phase between the input signal and the initial position of the system on the limit cycle. Noise sensitivity involves both spike-time jitter and transition probability. The resulting reliability map is strongly dependent on the details of the initial state.

Indeed, the presence and location of white areas as the ones in the suprathreshold panel of Fig. 2A is contingent on the detailed initial conditions, and also on the phase of the sinusoidal input. If the oscillatory input is implemented with a cosine function (instead of a sine), the location of such areas is displaced.

The inverse of the transition rates determines which recording intervals can be considered short, and which are long enough to reach the stationary situation. If the recording time is shorter than the inverse of both transition rates, reliability is likely to be low, since the evolution of a given trial depends critically on the particular realization of the noise, and on the phase of the oscillation in which the simulation is started. If the recording time is substantially longer than the inverse of one of the transition rates, but not the other, then the system behaves as entirely subthreshold, or entirely suprathreshold. Only when the recording time is substantially longer than the inverse of both transition rates, the stationary situation emerges. Initial conditions, hence, matter inasmuch as the stationary state is not yet reached.

8 Conclusion

Previous studies have proposed simple rules by which the input frequency producing maximally reliable spiking can be predicted. The rules depended on whether the neuron was clearly below or clearly above threshold. The present study explored the behavior of reliability at threshold, in bistable neurons. We showed that there is no simple rule that smoothly merges the optimal input frequency from $f_{\rm res}$ into $f_{\rm fir}$. Instead, at threshold both frequencies coexist, inducing a large variety of locking modes. These modes can explain the complexity observed in reliability maps. Similarly complex behaviors are expected to appear also in other bistable system endowed with two natural frequencies. As seen in Fig. 12, complexity fades progressively as transitions into one of the attractors become much more likely than into the others, as happens when we shift from the center of the bistable zone, moving away from threshold.

Bibliography

- Borkowski LS (2010) Multimodal transition and stochastic antiresonance in squid giant axons. Phys Rev E 82: 041909.
- Borkowski LS (2011) Bistability and resonance in the periodically stimulated Hodgkin-

Huxley model with noise. Phys Rev E 83: 051901.

- Bryant H, Segundo J (1976) Spike initiation by transmembrane current: a white-noise analysis. J Physiol (Lond) 260:279314.
- Buszaki G (2006) Rhythms of the brain. New York, Oxford University Press.
- Cecchi GA, Sigman M, Alonso JM, Martínez L, Chialvo D, Magnasco MO (2000) Noise in neurons is message dependent. Proc Natl Acad Sci U S A, 97(10):5557-61.
- Coombes S, Bressloff PC (1999) Mode locking and Arnold tongues in integrate-and-fire neural oscillators. Phys Rev E 60: 2086-2095.
- Coombes S, Owen MR (2001) Mode locking in a periodically forced integrate-and-fire-or-burst neuron model. Phys Rev E 64: 041914.
- Fellous JM, Houweling AR, Modi RH, Rao RP, Tiesinga PH, Sejnowski TJ (2001) Frequency dependence of spike timing reliability in cortical pyramidal cells and interneurons. J. Neurophysiol 85:1782-1787.
- Golomb D, Rinzel J (1993) Dynamics of globally coupled inhibitory neurons with heterogeneity. Phys Rev E 48: 4810-4814.
- Golomb D, Rinzel J (1994) Clustering in globally coupled phase oscillators. Phys Rev A 45: 3516-3530.
- Honeycutt RL (1992) Stochastic Runge-Kutta algorithms. I. White noise. Phys Rev A 45: 600-603.
- Hunter JD, Milton JG, Thomas PJ and Cowan JD (1998) Resonance effect for neural spike time reliability. J. Neurophysiol 80:1427-1438.
- Izhikevich EM (2007) Dynamical Systems in Neuroscience: The Geometry of Excitability and Bursting. The MIT Press, Cambridge, MA.
- Laing CR, Longtin A (2003) Periodic forcing of a model sensory neuron. Phys Rev E 67:051928.
- Mainen ZF, Sejnowski TJ (1995) Reliability of spike timing in neocortical neurons. Science 268: 1503-1506.
- Rowat PF, Greenwood PE (2011) Identification and Continuity of the Distributions of Burst-Length and Interspike Intervals in the Stochastic Morris-Lecar Neuron. N Comput 23: 30943124.

- Schreiber S, Fellous JM, Whitmer D, Tiesinga PHE, Sejnowski TJ (2003) A new correlation-based measure of spike timing reliability. Neurocomputing 52-4:925931.

- Schreiber S, Fellous JM, Tiesinga PHE, Sejnowski TJ (2004) Influence of ionic conductances on spike timing reliability of cortical neurons for suprathreshold rhythmic inputs. J Neurophys 91:194205.

- Schreiber S., Samengo I., & Herz A.V.M. (2009) Two distinct mechanisms shape the reliability of neural responses. J Neurophysiol 101: 2239-2251

- Tiesinga PHE (2002) Precision and reliability of periodically and quasiperiodically driven integrate-and-fire neurons. Phys Rev E 65: 041913.

- Tiesinga P, Fellous JM, Sejnowski TJ (2008) Regulation of spike timing in visual cortical circuits. Nat Rev Neurosci 9: 97-109.

- Tuckwell HC, Jost J (2010) Weak Noise in Neurons May Powerfully Inhibit the Generation of Repetitive Spiking but Not Its Propagation. PLoS Comput Biol 6(5): e1000794. doi:10.1371/journal.pcbi.1000794

- Tuckwell HC, Jost J, Gutkin BS (2009) Inhibition and modulation of rhythmic neuronal spiking by noise. Physical Review E 80, 031907.